Inflammation and Infection: Imaging Properties of ^{18}F-FDG–Labeled White Blood Cells Versus ^{18}F-FDG

Daniela Pellegrino, PhD[1,2]; Ali A. Bonab, PhD[2]; Stephen C. Dragotakes, BS[2]; Justin T. Pitman, BS[2]; Giuliano Mariani, MD[1]; and Edward A. Carter, PhD[2]

[1]Nuclear Medicine Division, Department of Oncology, University of Pisa Medical School, Pisa, Italy; and [2]Nuclear Medicine Division, Department of Radiology, Massachusetts General Hospital, Harvard Medical School, Boston, Massachusetts

^{18}F-FDG and ^{18}F-FDG–labeled white blood cells (^{18}F-FDG–WBCs) are valuable radiopharmaceuticals for imaging focal sites of inflammation and infection. In the present study, the imaging properties of both radiotracers were compared in sterile and septic inflammation models. **Methods:** Groups of adult male Sprague–Dawley rats (100–120 g) were injected in the left posterior thigh muscle with saline solution (group 1: controls, $n = 15$), 0.100 mL of turpentine oil (group 2: sterile inflammation, $n = 26$), 10^9 viable *Escherichia coli* bacteria (group 3: *E. coli* septic inflammation, $n = 29$), or 10^8 viable *Pseudomonas aeruginosa* bacteria (group 4: *P. aeruginosa* septic inflammation, $n = 25$). Twenty-four hours later, the animals were divided into 2 groups: One received ^{18}F-FDG intravenously and the other received human white blood cells (WBCs) labeled in vitro with ^{18}F-FDG injected intravenously. Biodistribution and microPET studies were performed 1 h after radiotracer injection. One hour after injection with cell-associated or free ^{18}F-FDG, phosphorimaging of abscess and contralateral muscle was performed in specimens collected from animals in groups 1, 2, and 3. The region of interest was selected within the abscess wall and values were converted to kBq/g using a ^{14}C calibration standard curve. Thin-layer radiochromatography (TLRC) was performed to study the chemical forms of ^{18}F within the WBCs. **Results:** Whole-body biodistribution demonstrated a significantly higher uptake ratio of ^{18}F-FDG–WBCs compared with ^{18}F-FDG in all sterile and septic inflammation models (*t* test: sterile, $P = 0.048$; *E. coli*, $P = 0.040$; *P. aeruginosa*, $P = 0.037$). microPET imaging confirmed the greater performance of ^{18}F-FDG–WBCs versus ^{18}F-FDG in the sterile inflammation model and in both *E. coli* and *P. aeruginosa* septic models. Phosphorimaging analysis showed higher ^{18}F-FDG–WBC uptake than ^{18}F-FDG in the sterile inflammation and *P. aeruginosa* septic models and similar tissue uptake in the *E. coli* septic model. Time course labeling and TLRC of lysed WBCs demonstrated that ^{18}F-FDG was retained as ^{18}F-FDG-6-phosphate inside WBCs for at least 2 h, corresponding to the time frame of analysis. **Conclusion:** ^{18}F-FDG–WBCs gave better results compared with ^{18}F-FDG in all sterile and septic inflammation models. These data suggest that ^{18}F-FDG–WBC PET may be a useful technique for tracking focal inflammatory lesions in the body.

Key Words: ^{18}F-FDG–labeled white blood cells; infection; inflammation; biodistribution; microPET; phosphorimaging

J Nucl Med 2005; 46:1522–1530

Detection and localization of infectious and noninfectious foci in soft tissues is of primary importance for the management of patients with presumed or established inflammatory and septic diseases. Ultrasound, CT, and MRI are effective in detecting inflammation whenever the lesion has caused changes in local anatomy, capillary permeability, or tissue water content (*1*). When normal anatomic landmarks are lost or obscured, localization of inflammatory foci can best be accomplished with scintigraphic techniques.

Sterile and septic inflammatory processes develop through a cascade of events, characterized by a local increase of blood supply, small molecules, and proteins, leakage of fluids, and infiltration of inflammatory cells (*2*). Within a few hours of the insulting event, granulocytes accrue in the damaged tissue, begin phagocytosis, and release chemoattractant molecules for monocytes and monocyte-derived macrophages that soon become the predominant cell subset. Among other functions, these cells also phagocytize cell debris, live and dead bacterial cells, and apoptotic granulocytes. This process usually precedes resolution of the inflammation process (*3*). ^{111}In- or ^{99m}Tc-labeled white blood cell (WBC) scintigraphy is a routine procedure for localizing inflammation (*4–6*), as these radiotracers allow visualization of inflammatory foci in a few hours (*7*).

PET with ^{18}F-FDG is also useful to detect infection and inflammation foci (*8*), as these sites are seen as regions of increased ^{18}F-FDG uptake on the scan. Recently, WBCs labeled with ^{18}F-FDG (^{18}F-FDG–WBCs) have been suggested as a radiotracer for imaging inflammation foci (*9*). The performance of labeled WBC imaging depends on

several variables, such as the intensity of the neutrophilic component of the inflammatory response and, consequently, production of the inflammation chemotactic signal (10,11). This method has several potential advantages, including higher sensitivity and specificity than intravenous ^{18}F-FDG.

This study was performed to compare the relative uptakes of intravenously injected ^{18}F-FDG and of ^{18}F-FDG–labeled WBCs in sterile and septic inflammation foci in an animal model.

MATERIALS AND METHODS

Animals and Experimental Design

The sterile and septic inflammation studies were performed with a starting total of 105 male Sprague–Dawley rats (Charles River Laboratories). Care was performed in accordance with the guidelines outlined in *Guide for the Care and Use of Laboratory Animals* (12). Animals, 6- to 8-wk old and 100–120 g in weight, were divided in the following groups: 15 rats as the control group and 30 rats each for the sterile inflammation, *Escherichia coli* infection, and *Pseudomonas aeruginosa* infection models, respectively. However, some of the animals receiving the inflammatory/infectious agents died before completion of the experiments, so that the final composition of the experimental groups was as follows: group 1 (control), 15 rats receiving saline (9 biodistribution, 6 microPET imaging [Concorde Microsystems Inc.]); group 2 (sterile inflammation), 26 rats receiving turpentine oil injection (12 biodistribution, 6 microPET imaging, 8 phosphorimaging); group 3 (*E. coli* septic inflammation), 29 rats receiving *E. coli* injection (12 biodistribution, 6 microPET imaging, 11 phosphorimaging); group 4 (*P. aeruginosa* septic inflammation), 25 rats receiving *P. aeruginosa* injection (12 biodistribution, 6 microPET imaging, 7 phosphorimaging) (Table 1). As outlined in Figure 1, 24 h after inoculation of the septic/aseptic inflammation agents, rats were injected intravenously with ^{18}F-FDG or ^{18}F-FDG–WBCs. One hour later, the rats were subjected to biodistribution, microPET imaging, and phosphorimaging.

Sterile and Septic Inflammation Agents

Aseptic inflammation was induced with 100 μL of 100% pure turpentine oil ($C_{10}H_6$) (Fisher Scientific) and septic inflammation was induced with 2 clinical isolates of *E. coli* or *P. aeruginosa*. These 2 bacterial strains were chosen because they are highly prevalent in nosocomial infections and, especially the latter, a major source of morbidity and mortality. Briefly, 30 μL of a frozen stock of *E. coli* and *P. aeruginosa* bacterial cells was grown at 37°C in Luria–Bertani medium (Sigma) and overnight cultures were diluted up to $OD_{600} = 0.5$ (middle-logarithmic phase). The resulting bacterial suspension was spun down, washed with 0.9% NaCl, resuspended to reach a concentration of 10^{10} bacterial cells/mL, and inoculated (100 μL) into rats. Inflammatory/infectious agents were inoculated into the left thigh muscle (25-gauge needle) under Halothane anesthesia (Halocarbon Laboratory). Animals then fasted overnight under the standard condition of light and free access to water. All animals developed an abscess detectable as a palpable fluctuant mass within 24 h after oil or bacteria inoculation.

Synthesis of ^{18}F-FDG

^{18}F-FDG was prepared with computer-aided synthesis (Nuclear Interface) by nucleophilic substitution via a modified Hamacher reaction (13).

^{18}F-FDG Labeling of Human WBCs

Fresh circulating WBCs were isolated from 20–40 mL of peripheral venous blood collected on the day of the experiment from a healthy, fasted human volunteer (the same individual for all experiments) in 200–400 U of heparin. Initial screening indicated that the volunteer's fasting blood glucose level was within physiologic range (75 mg/dL), as also was the total WBC count with differential count (5,600/μL with 65.3% neutrophils, 24.5% lymphocytes, 5.4% monocytes, 1.4% eosinophils, 0.6% basophils), thus confirming the donor's healthy condition. After gravity sedimentation in a 50-mL Falcon tube (Becton Dickinson Labware) in 6% Hetastarch (Baxter Health Care Corp.), pelleted WBCs was resuspended in 0.5 mL of 0.9% NaCl and 74–148 MBq of ^{18}F-FDG were added. The WBCs were incubated at 37°C in a lead-lined incubator for 20 min under gentle continuous shaking. The labeling reaction was stopped by adding chilled human cell-free serum, and labeled WBCs were washed twice in 0.9% NaCl to separate free from bound ^{18}F-FDG (14). The percentage labeling efficiency was measured using a well-type ionization dose calibrator (Radioisotope Calibrator CRC-II; Capintec Inc.) and determined as the activity bound to cells compared with the total activity measured.

Labeling Efficiency, Cell Viability, and Thin-Layer Radiochromatography (TLRC)

The efficiency of WBC labeling and the chemical form of intracellular trapped ^{18}F were evaluated at 90, 150, and 240 min after completion of the labeling reaction. Over this period, cells were kept in 0.9% NaCl at 37°C under gentle continuous shaking as for the labeling reaction. At those time points, 10 μL of the

TABLE 1
Experimental Groups Undergoing ^{18}F-FDG–WBC and ^{18}F-FDG Biodistribution, microPET, and Phosphorimaging Study

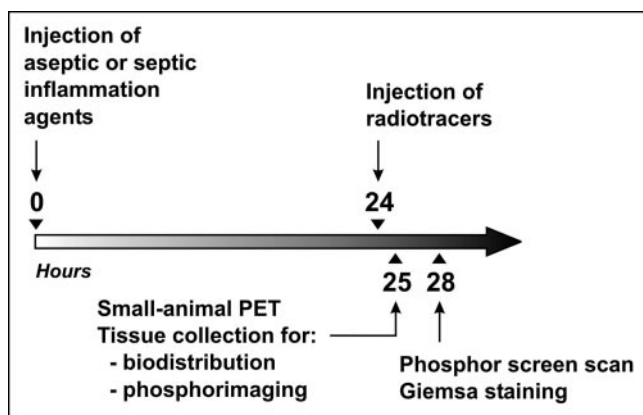| Group	No. of animals	Biodistribution ^{18}F-FDG–WBC	Biodistribution ^{18}F-FDG	microPET ^{18}F-FDG–WBC	microPET ^{18}F-FDG	Phosphorimaging ^{18}F-FDG–WBC	Phosphorimaging ^{18}F-FDG
1 Control							
	15	4	5	3	3	—	—
2 Sterile inflammation (turpentine)							
	26	6	6	3	3	4	4
3 Septic inflammation (*E. coli*)							
	29	6	6	3	3	6	5
4 Septic inflammation (*P. aeruginosa*)							
	25	6	6	3	3	4	3

FIGURE 1. Outline of experimental design.

labeled cell suspension were mixed in a trypan blue-saline solution (Sigma). Ten microliters of the mixture were placed in a hemocytometer chamber and the number of cells with and without stain was counted. Cell viability at each time point was calculated as the percentage of unstained cells per total cells (*15*).

The TLRC standard, ^{18}F-FDG-6-phosphate (^{18}F-FDG-6P), was synthesized by adding ^{18}F-FDG (1.85 MBq) to a master mix reaction mixture (pH 8.0) containing hexokinase (48 U; Sigma), adenosine triphosphate (50 mmol/L), and $MgCl_2 \cdot H_2O$ (100 mmol/L; Sigma). The reaction was incubated for 45 min at 33°C (*16*). To evaluate the chemical status of the radiotracer within WBCs, aliquots of labeled cells were collected at 90, 150, and 240 min after labeling, washed, and lysed with Zap-Oglobin II Lytic Reagent (Coulter Electronics, Beckman Coulter Co.). Cell lysate was then washed and spotted together with ^{18}F-FDG-6P and ^{18}F-FDG standards on aluminum silica gel thin-layer chromatography strips (20 × 20 cm × 254 nm; EM Science). Chromatographic separation was performed by using an acetonitrile/water mixture solvent (95:5 v/v) in a developing chamber. Chromatography strips were dried and activity was counted using a Bioscan System AR-2000 scanner to determine the relative activities of ^{18}F-FDG and ^{18}F-FDG-6P.

Whole-Body Biodistribution

Rats were injected with 2.9–3.7 MBq of radiotracer (^{18}F-FDG or ^{18}F-FDG–WBCs) via tail vein and sacrificed by CO_2 asphyxiation after 1 h. Animals were then dissected, blood was collected, and various organs were excised and weighed. Radiotracer activity was determined by using a γ-counter (Wallac 1480; Perkin Elmer). The percentage injected dose per gram (% DPG) was determined and decay corrected for each sample. The radioactivity content of tissue samples was calibrated against 2% standard injected activity. Results are expressed as % DPG of infected muscle-to-normal muscle ratio (IM/NM ratio) ± SE and corrected for background and decay.

microPET

Imaging studies were performed with 3 rats per group examined in parallel. One hour before scanning, 7.7–11.8 MBq of radiotracer (^{18}F-FDG or ^{18}F-FDG–WBCs) were administered intravenously via tail vein. Ten minutes before scanning, animals were anesthetized by a single intraperitoneal injection of ketamine-xylazine mixture (ketamine, 50 mg/kg; xylazine, 5 mg/kg). PET static images were acquired by using a P4 microPET system (Concorde

Microsystems Inc.) without attenuation correction over a 15-min period. The images were reconstructed using filtered backprojection (2.2-mm resolution) and analyzed by manually drawing adequate regions of interest (ROIs) within the right (uninfected) and left (infected) thigh muscle. The ^{18}F-FDG and ^{18}F-FDG–WBC uptake on the PET images was expressed as the IM/NM count ratio within each corresponding paired ROI, uncorrected for tissue attenuation.

Phosphorimaging of Frozen Sections

Distribution of radiotracers in the infected muscle tissue was evaluated using phosphorimaging. One hour after radiotracer injection, muscles (infected and contralateral) were removed and quickly frozen in isopentane precooled in liquid nitrogen and then embedded in an optimal-cutting temperature compound (Sakura Finetek) to obtain frozen sections (Ames Cryostat II; Spectron Corp.).

In a calibration experiment, slices from rat brain paste were prepared to obtain a calibration curve for ^{18}F against ^{14}C standards (ARC-146; American Radiolabeled Chemicals). Several freshly harvested brains were homogenized and part of the minced tissue was mixed thoroughly with a defined amount of ^{18}F-FDG and then serially diluted with cold brain paste to obtain scaled amounts of ^{18}F-FDG (0.024–16.6 MBq). The labeled paste was then centrifuged and sliced at 14-μm thickness and transferred to glass slides (Superfrost/Plus; Fisher Scientific). The ^{18}F-FDG-labeled brain slices were then placed in an exposure Phosphorimager Cassette (Molecular Dynamics, Pharmacia Biotech) together with ^{14}C standard slices for 4 h at room temperature. After exposure, the phosphor screen images were read out for 31 min at a resolution of 50 μm per pixel in a Storm System 860 optical scanner (Molecular Dynamics). Images were then digitized in black-white scale, and the gray values were converted into kBq per gram (kBq/g) using the calibrated standards. The activities were then decay corrected for time elapsed since sample preparation. ^{18}F-FDG activity was plotted against measured values and the curve was then generated using linear curve-fitting regression. Subsequently, the ^{14}C measured activity (kBq/g) was then calibrated using the ^{18}F-FDG curve to obtain the ^{14}C standard calibration curve (*17*).

The measured tissue activity/gram (kBq/g) was extrapolated by the ^{14}C standard calibration curve. Finally, ROIs were placed on the abscess wall (IM) and the contralateral muscle to quantify ^{18}F-FDG and ^{18}F-FDG–WBC uptake, using Imaging Quant Software, version 2.1 (Molecular Dynamics). Results were calculated as standard uptake values (SUVs) using a standard formula including injected dose and body weight of the animal (*18,19*). For easier comparison, all data were then expressed as the ratio of SUVs ± SE between IM and NM.

Histology

Fourteen-micrometer frozen sections were stained with 10% Giemsa (Fisher Scientific); slices were identified by a random code number and analyzed by a pathologist who was unaware of the specific experiment.

Statistical Analysis

Differences between groups were tested for statistical significance using the Student unpaired 2-tail *t* test assuming equal variances. *P* values of less than 0.05 were considered significant. Results are expressed as mean ± SE.

RESULTS

18F-FDG Labeling and Biochemical Analysis of WBCs

The ^{18}F-FDG labeling procedure of WBCs harvested from the healthy volunteer did not induce appreciable damage to the cells, as they were found to be 98.5%–99.9% and 84%–87% viable at 90 and 240 min after labeling, respectively.

WBC labeling efficiency with ^{18}F-FDG after the 20-min incubation was in the 64%–75% range. When the WBCs were kept in the labeling mixture for extended period of time (without any further washing), the fraction of cell-bound radioactivity decreased from that initial value to 39%–44% at 90 min and eventually to 19% at 240 min (Fig. 2A).

Chromatograms of cell lysates showed that at both 90 and 240 min, most of the intracellular radioactivity (98%) had the same retention factor ($R_f = 0$) of the ^{18}F-FDG-6P standard. Only minimal amounts of ^{18}F-FDG (about 2% radioactivity with an $R_f = 0.37$) were found in the intracellular compartment at the same time points (Fig. 2B).

18F-FDG–WBCs Versus 18F-FDG Uptake in Control Rats

Biodistribution analysis showed similar radioactivity contents in the compartment of interest (muscle) for ^{18}F-FDG–WBCs and for ^{18}F-FDG in the control rats without induced inflammation. The only noticeable difference between the biodistribution of the 2 tracers in the control rats was accumulation of ^{18}F-FDG–WBCs in the lungs, liver, and spleen higher than that of ^{18}F-FDG, a well-known, physiologic phenomenon commonly observed also when performing imaging studies with radiolabeled WBCs in patients (*19*). Both biodistribution and microPET studies showed that this expected pattern of differential biodistribution in the lungs, liver, and spleen between ^{18}F-FDG–WBCs and ^{18}F-FDG injected as such was maintained throughout the control rats and the groups of animals with sterile or septic inflammation (data not shown).

18F-FDG–WBCs Versus 18F-FDG Uptake in Sterile Inflammation

Biodistribution. Localization of inflammation foci gave different results depending on the radiotracer and the method used for its detection. By using whole-body biodistribution analysis, accumulation of both agents in the inflamed muscle was at least 12-fold higher than that in the noninflamed muscle. Significantly higher uptake of ^{18}F-FDG–WBCs compared with ^{18}F-FDG was found in lungs ($P = 0.02$) and testes ($P = 0.026$), whereas it was lower in brain ($P = 0.0039$) and gastrointestinal tract ($P = 0.0031$) (Fig. 3A). Importantly, the % DPG IM/NM ratio showed a significantly higher recruitment of ^{18}F-FDG–WBCs in inflamed muscle compared with ^{18}F-FDG uptake ($P = 0.048$; Table 2).

microPET. On microPET imaging, both radiotracers exhibited fairly high uptake in liver, spleen, bone marrow, and bladder and very low uptake in normal muscle. Compared with ^{18}F-FDG alone, ^{18}F-FDG–WBCs showed lower uptake in brain, most likely due to the limited diffusion through the blood–brain barrier (BBB). Inflamed muscle showed very high uptake of both radiotracers as compared with normal contralateral tissue (Fig. 3B). Similarly, as in the biodistribution studies, ^{18}F-FDG–WBCs better discriminated between inflamed and normal tissue, as shown by the significantly higher IM/NM uptake ratios compared with ^{18}F-FDG (19.71 ± 0.38 vs. 8.04 ± 0.59, $P < 0.001$) (Table 2).

Phosphorimaging. On phosphorimaging analysis, both radiotracers were mainly localized within close proximity of or within cell infiltrates that were confirmed to be granulocytes by Giemsa staining of tissue sections (Fig. 3C). SUVs in the inflamed sites, calculated from the phosphorimaging-built autoradiographic images (ROIs selected within the wall of the abscess and the contralateral muscle Fig. 3D), were distinctly higher for ^{18}F-FDG–WBCs (21.81 ± 3.91) than for ^{18}F-FDG (12.85 ± 1.11) (Table 2).
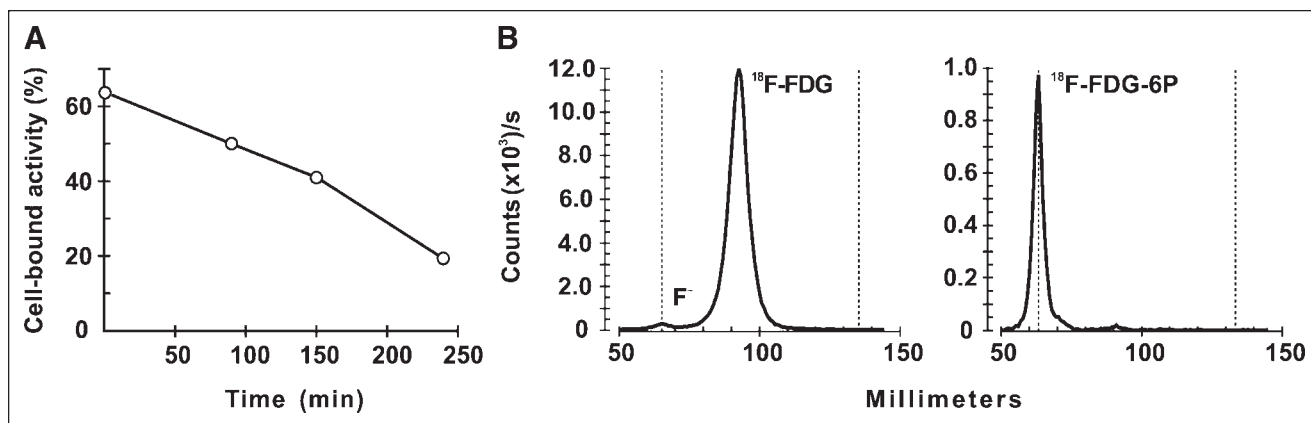

FIGURE 2. (A) Time course retention of ^{18}F-FDG in WBCs incubated in 0.9% NaCl for extended periods at 37°C. Percentage cell-bound activity (labeling) is expressed as pellet activity/total activity ratio. (B) TLRC at 90 min after WBC labeling. Dotted lines indicate retention factor, $R_f = 0$ (left) and $R_f = 1$ (right). Center panel: ^{18}F-FDG ($R_f = 0.37$) contains trace of ^{18}F-fluoride not migrating with the mobile phase. Right panel: Lysed ^{18}F-FDG–WBCs (similarly as ^{18}F-fluoride, ^{18}F-FDG-6P used as standard does not migrate with the mobile phase).
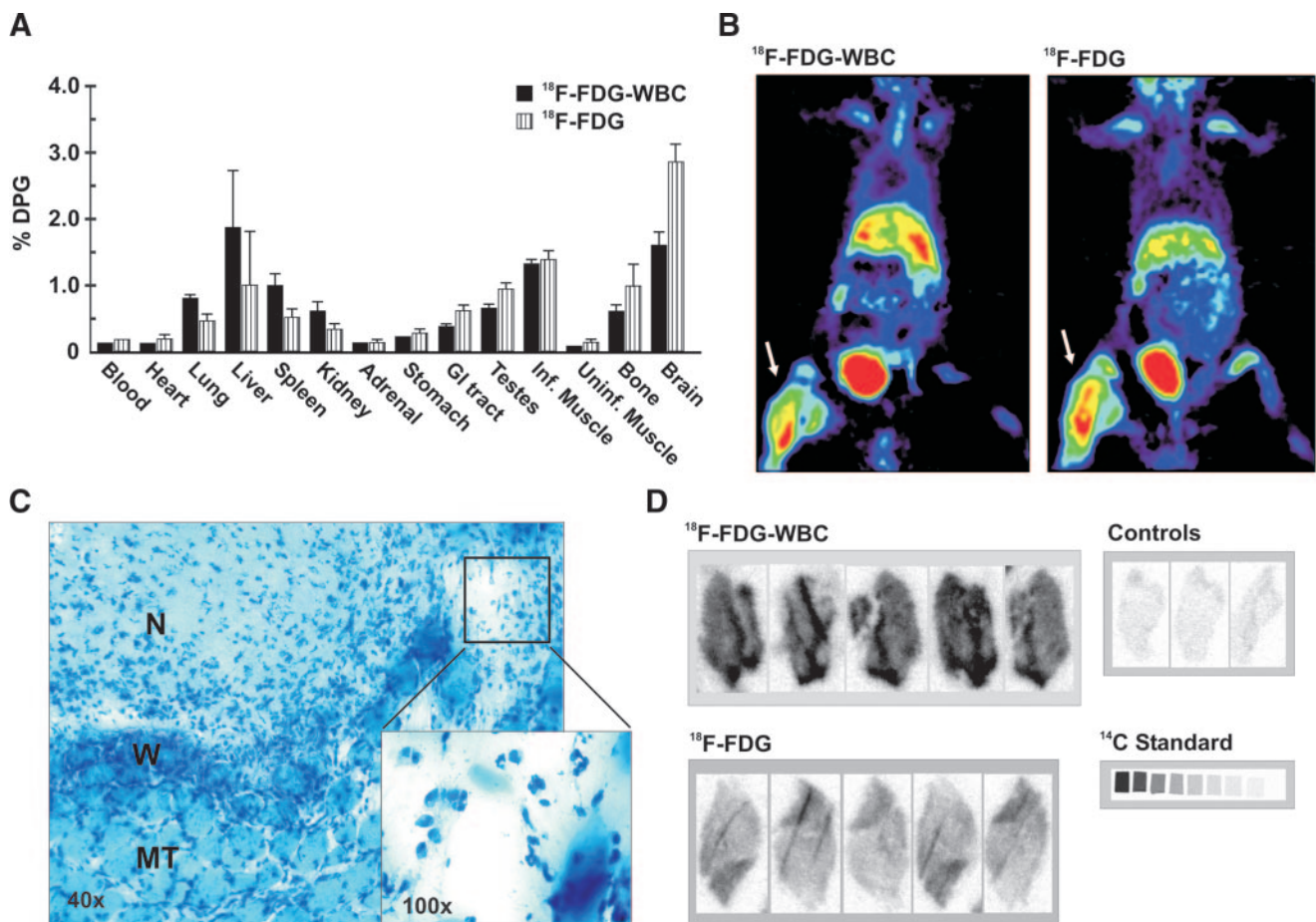
FIGURE 3. (A) Tissue biodistribution of ^{18}F-FDG–WBCs and ^{18}F-FDG in turpentine model 1 h after radiotracer injection. Values are expressed as % DPG (mean ± SE). (B) Coronal images of turpentine model obtained 1 h after radiotracer injection. Arrow indicates inflammation site (animals positioned prone on imaging table). (C) Microscopic images of Giemsa-stained sterile inflamed muscle sample, collected 1 h after radiotracer injection. Abscess is characterized by central necrosis (N) and a surrounding wall (W) mainly consisting of granulocytic cells and normal muscle tissue (MT). (D) Phosphorimaging of frozen section from turpentine-injected muscle (IM) and normal muscle (NM), collected 1 h after radiotracer injection. Standard: [14]C standard activity values were converted to ^{18}F activity in MBq/g by using a calibration curve. Control: NM ^{18}F-FDG–WBC, tissue uptake = 0.22 kBq/g. ^{18}F-FDG–WBC: IM ^{18}F-FDG–WBC, tissue uptake = 8.14 kBq/g. ^{18}F-FDG: IM ^{18}F-FDG, tissue uptake = 3.07 kBq/g. DPG = (injected dose/gram of tissue) × 100; GI = gastrointestinal; Inf. = infected; Uninf. = uninfected.

Histology

Giemsa staining of the inflamed muscle specimens excised 24 h after turpentine injection showed massive neutrophil infiltration in necrotic muscle fibers surrounded by inflammatory cells (Fig. 3C).

^{18}F-FDG–WBCs Versus ^{18}F-FDG Uptake in *E. coli* Septic Inflammation

Biodistribution. Similar organ uptakes were observed for the 2 radiotracers with the exception of lungs, kidneys, and gastrointestinal tract, where ^{18}F-FDG–WBC uptake was much higher than ^{18}F-FDG alone ($P = 0.00004–0.00006$) (Fig. 4A); similarly, as in the other models, uptake of ^{18}F-FDG in brain was higher than ^{18}F-FDG–WBC uptake ($P = 0.011$). It should also be noted that in these organs the uptake of both radiotracers was higher than in the sterile inflammation model. This pattern might indicate that the *E. coli* infection started to spread within the body. The % DPG IM/NM ratio for ^{18}F-FDG–WBCs was significantly higher than for ^{18}F-FDG ($P = 0.040$, Table 2).

microPET. microPET imaging showed slightly higher uptake in liver, spleen, genitourinary system, and bone marrow and lower uptake in brain for ^{18}F-FDG–WBCs compared with ^{18}F-FDG. Differences were even more noticeable when imaging infected and normal tissue. As expected from biodistribution values, high uptake was observed in the *E. coli*-infected muscle for both radiotracers (Fig. 4B). Finally, the ^{18}F-FDG–WBCs IM/NM ratio was significantly higher than for ^{18}F-FDG ($P < 0.001$, Table 2).

Phosphorimaging. Localization of both radiotracers by phosphorimaging analysis showed a heterogeneous pattern as the abscess centers contained areas with very low radioactivity or virtually devoid of radiotracer uptake. On Giemsa-stained tissue sections, these areas were surrounded by an inner layer of cell and bacterial debris and an outer

TABLE 2
Summary of IM/NM Ratios

Group	Biodistribution* 18F-FDG–WBC	18F-FDG	microPET† 18F-FDG–WBC	18F-FDG	Phosphorimaging‡ 18F-FDG–WBC	18F-FDG
1 Sterile inflammation (turpentine)						
	24.24 ± 3.98	12.21 ± 3.68	19.71 ± 0.38	8.04 ± 0.59	21.81 ± 3.91	12.85 ± 1.11
	$P = 0.048$		$P < 0.001$		NS	
2 Septic inflammation (E. coli)						
	14.67 ± 1.85	10.04 ± 0.66	26.61 ± 0.04	12.35 ± 0.01	25.27 ± 3.97	20.70 ± 3.43
	$P = 0.040$		$P < 0.001$		NS	
3 Septic inflammation (P. aeruginosa)						
	15.62 ± 4.30	5.08 ± 0.93	10.89 ± 0.12	4.35 ± 0.09	10.11 ± 1.33	5.57 ± 0.43
	$P = 0.037$		$P < 0.001$		$P < 0.01$	

*% DPG of IM/NM ± SE, corrected for background and decay.
†IM/NM ± SE.
‡Defined as SUV ratio of IM/NM ± SE.
NS = not significant.

layer of neutrophils. On histologic examination, the central area of the acute abscess was confirmed to be predominantly necrotic and surrounded by neutrophils and other inflammatory cells, mostly granulocytes. The surrounding layers were characterized by strong radiotracer uptake that clearly depicted and paralleled the localization of neutrophils (Fig. 4C). SUVs calculated from ROIs containing the abscess wall (Fig. 4D) showed distinctly higher 18F-FDG–WBC uptake that performed better than 18F-FDG uptake in terms of the IM/NM ratio (Table 2).

Histology

Giemsa staining of the inflamed muscle specimens excised 24 h after E. coli injection showed that the central area of the abscess was surrounded by an inner layer of cell and bacterial debris and by an outer layer of neutrophils (Fig. 4C).

18F-FDG–WBC Versus 18F-FDG Uptake in P. aeruginosa Septic Inflammation

Biodistribution. The 2 radiotracers showed similar organ biodistribution and uptake as in the E. coli septic model (Fig. 5A). The 18F-FDG–WBCs % DPG IM/NM ratio was found to be 3-fold higher than that of 18F-FDG alone ($P = 0.037$, Table 2).

microPET. microPET imaging showed slightly higher uptake in liver, spleen, genitourinary system, and bone marrow (Fig. 5B) and lower uptake in brain for 18F-FDG–WBCs compared with 18F-FDG (not shown). Differences were even more noticeable when imaging infected and normal muscle tissue. As for the E. coli infection model, 18F-FDG–WBC uptake in P. aeruginosa-infected muscle was significantly higher compared with 18F-FDG ($P < 0.001$, Table 2).

Phosphorimaging. Phosphorimaging analysis of radiotracers in the P. aeruginosa-infected animals gave results that were superimposable on E. coli results (data not shown). However, as expected by the higher pathogenicity of the former bacteria, the tissue architecture was heavily damaged and Giemsa staining did not prove useful for identifying the inflammatory cells. Finally, 18F-FDG–WBCs showed a higher IM/NM ratio compared with 18F-FDG ($P < 0.01$, Table 2).

Histology

On histologic examination, the tissue architecture was heavily disrupted and, as expected because of the intense pathogenicity of this bacterial strain, Giemsa staining did not prove useful for identifying intact inflammatory cells (Fig. 5C).

DISCUSSION

The cell subsets intervening in inflammatory and septic processes are normally neutrophils and macrophages that are attracted by a variety of stimuli released at the site of the lesion (20). These cells are metabolically active and, therefore, consume large quantities of glucose. High tissue radioactivity after administration of 18F-FDG corresponds to increased glucose uptake and consumption through the hexose monophosphate shunt, the main source of energy in chemotaxis and phagocytosis (21). Activation of phagocytes, also known as respiratory burst activation, similarly leads to increased 18F-FDG uptake (22).

Our experiments were performed using an animal model of infection and inflammation. Under such controlled and standardized conditions, abscesses were detected and localized 24 h after induction by either 18F-FDG or 18F-FDG–WBCs.

Imaging and biodistribution studies were performed 1 h after injection of the radiolabeled agents, a time frame chosen to mirror the clinical setting when using 18F for PET. Biodistribution analysis and phosphorimaging, used in parallel with microPET imaging, essentially yielded the same
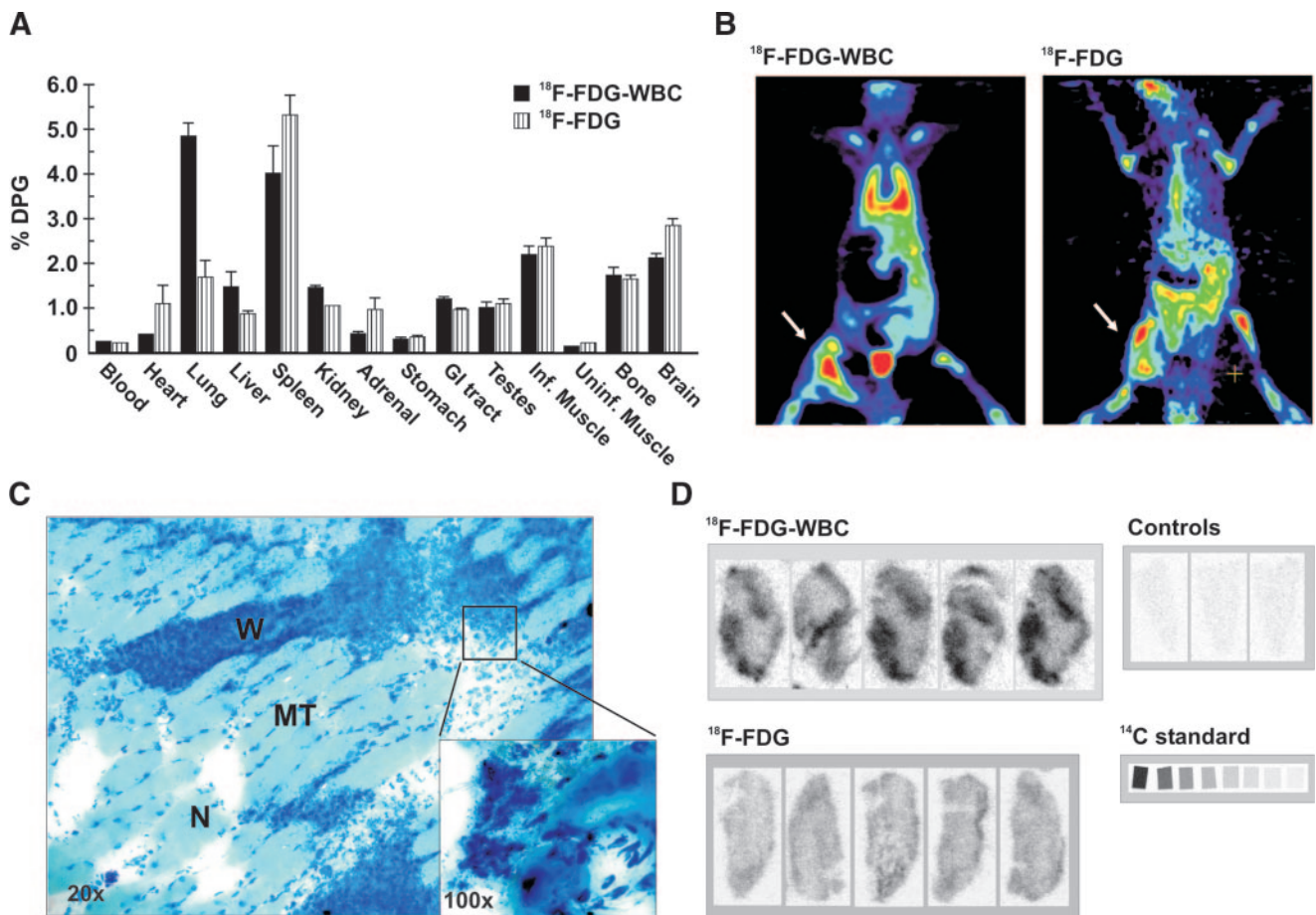
FIGURE 4. (A) Tissue biodistribution of ^{18}F-FDG–WBCs and ^{18}F-FDG in *E. coli* model 1 h after radiotracer injection. Values are expressed as % DPG (mean ± SE). (B) Coronal images of *E. coli* model obtained 1 h after radiotracer injection. Arrow indicates infection site (animals positioned prone on imaging table). (C) Microscopic images of Giemsa-stained *E. coli*-injected septic muscle sample, collected 1 h after radiotracer injection. Necrosis (N) and abscess architecture showed a different organization compared with the sterile model. Numerous inflammatory cells were present in surrounding wall (W) infiltrating muscle tissue (MT). *E. coli* can be seen in the higher magnification. (D) Phosphorimaging of frozen section from *E. coli*-infected muscle (IM) and normal muscle (NM), collected 1 h after radiotracer injection. Standard: ^{14}C standard activity values were converted to ^{18}F activity in MBq/g by using a calibration curve. Control: NM ^{18}F-FDG–WBC, tissue uptake = 0.1 kBq/g. ^{18}F-FDG–WBC: IM ^{18}F-FDG–WBC, tissue uptake = 2.035 kBq/g. ^{18}F-FDG: IM ^{18}F-FDG, tissue uptake = 0.99 kBq/g. DPG = (injected dose/gram of tissue) × 100; GI = gastrointestinal; Inf. = infected; Uninf. = uninfected.

results and confirmed the superior performance of ^{18}F-FDG–WBCs versus ^{18}F-FDG for detecting the inflammation foci. As also reported in other studies (*23,24*), human WBCs were used in the present study—instead of homologous, rat WBCs—because of easy collection and a large supply without the need to use many animals for WBC preparation. Previous experiments performed by Osman and Danpure (*25*) demonstrated that, after incubating ^{18}F-FDG with the WBC pellet, most of the tracer (87%) was associated with granulocytes, whereas a minor fraction was associated with monocytes, lymphocytes, platelets, and erythrocytes. Therefore, because granulocytes are the chief inflammatory cells involved in acute infection (*26*), the appropriateness of labeling the entire WBC pool for detecting inflammatory foci is confirmed.

As demonstrated by Yamada et al., in sterile inflammation ^{18}F-FDG administered as such is mainly taken up in neutrophils and macrophages (*27*), with the highest ^{18}F-FDG uptake being seen in neutrophils during the acute phase of inflammation (*17*) and in macrophages and polymorphonuclear leukocytes during the chronic phase (*28*). It should be mentioned, however, that no difference in ^{18}F-FDG uptake between infected and normal muscle has occasionally been reported, although increased ^{18}F-FDG uptake in abscess has definitely been observed in humans (*29*). Our experience in setting up the experimental animal models described here confirms that special attention must be paid to standardize as much as possible the various phases of the procedures, such as (a) physical status and fasting of treated animals, (b) number of labeled WBCs reinfused, (c) fasting condition of the donor at time of blood withdrawal, and (d) number and growth phase at which bacteria were collected for inoculation in animals. In general, live bacteria collected during the logarithmic growth phase induced more
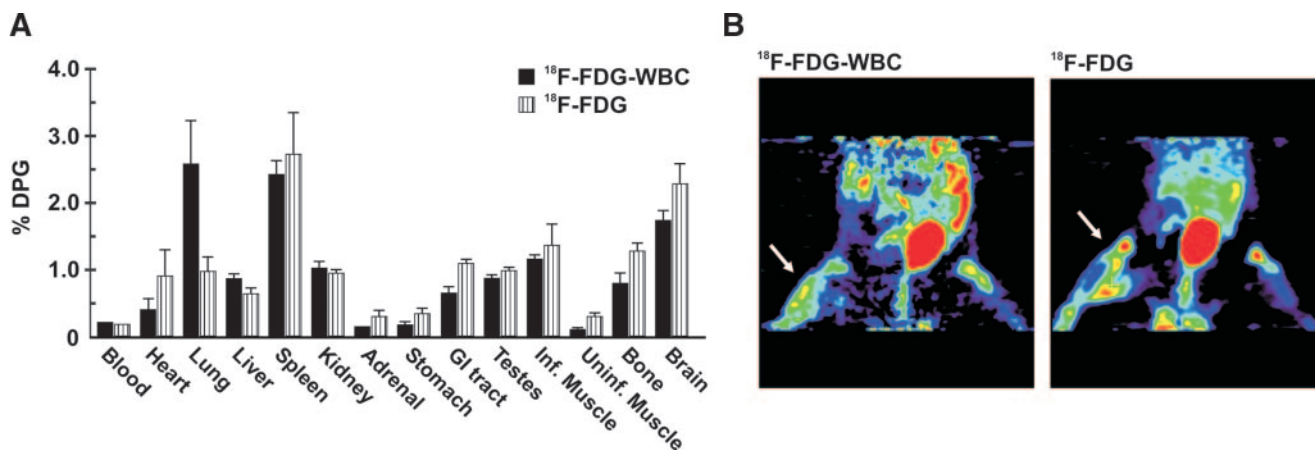
FIGURE 5. (A) Tissue biodistribution of ^{18}F-FDG–WBCs and ^{18}F-FDG in *P. aeruginosa* model 1 h after radiotracer injection. Values are expressed as % DPG (mean ± SE). (B) Coronal images of *P. aeruginosa* model obtained 1 h after radiotracer injection. Arrow indicates infection site (animals positioned prone on imaging table). DPG = (injected dose/gram of tissue) × 100; GI = gastrointestinal; Inf. = infected; Uninf. = uninfected.

clearly visible and consistent septic abscesses than bacteria collected at a plateau of growth. In addition, animals that were left fasting for 16–24 h before inoculation with radiotracers showed higher nonspecific uptake and a reduced signal-to-noise ratio (data not shown).

Acute inflammation induced by sterile or bacterial agents was observed 24 h after injection, when the left thigh muscle exhibited clear signs of acute inflammation (redness and swelling). In these conditions, the radiotracer localization visualized by microPET was confirmed both by the "gold standard" biodistribution study and by phosphorimaging analysis. With only marginal differences, the microPET and phosphorimaging results clearly parallel the biodistribution study, with all 3 methods consistently showing markedly higher uptake of both radiotracers in the infected muscle compared with the contralateral site and with average ^{18}F-FDG–WBC IM/NM ratios approximately twice as high as the ^{18}F-FDG IM/NM ratios.

To ascertain that labeled WBCs still incorporated ^{18}F-FDG when analyzed for tissue biodistribution, time-course viability experiments were performed. Initial postlabeling and viability of WBCs (99.9% at 20 min) was very high and was comparable to that found with ^{99m}Tc and ^{111}In labeling of WBCs (*30*). This parameter did not appreciably change throughout the potential time window useful for PET (90 min). The chemical form of ^{18}F was also analyzed by TLRC to establish whether the ^{18}F-FDG was actually retained within cells throughout the duration of the study. TLRC analysis demonstrated that virtually all radioactivity inside the WBCs was present as ^{18}F-FDG-6P, a chemical form incapable of egression from the cell and minimally reconverted to ^{18}F-FDG.

In the sterile inflammation model, both radiotracers were primarily localized within close proximity or within cells infiltrates that Giemsa staining confirmed to be granulocytes. In the septic inflammation model, the surrounding layers were characterized by strong radioactivity uptake that

clearly depicted and mimicked the localization of neutrophils.

Histologic analysis also confirmed gross infiltration of granulocytes and macrophages in the inflamed/infected muscle tissue. These findings suggest that the increased performance of ^{18}F-FDG–WBCs was due to sensitization and recruitment of labeled cells by the chemoattracting factors released into and around the inflammation areas. This possibility, combined with the fact that similar amounts of ^{18}F-FDG or ^{18}F-FDG–WBCs were administered and that human labeled WBCs did not release significant amounts of ^{18}F-FDG within 1 h after injection, indicated that ^{18}F-FDG–WBCs' focal uptake is a specific phenomenon and not the result of nonspecific accumulation of free ^{18}F-FDG.

Uptake ratios of ^{18}F-FDG and ^{18}F-FDG–WBCs differed in the tissues analyzed. microPET imaging showed high accumulation of ^{18}F-FDG–WBCs in the lungs, an observation in line with common findings observed in humans with radiolabeled WBCs (*19*). Because neutrophils are not activated in normal conditions but can undergo activation during the labeling procedure as a result of cell trauma (*31*), high physiologic uptake of ^{18}F-FDG–WBCs might be due to changes in the cytoskeleton of neutrophils (*32,33*). This would lead to formation of stiffer cellular membranes that adhere to the pulmonary capillaries while traveling through the pulmonary vessels. Such high physiologic uptake, also defined "margination" (*34*), should therefore be considered as it could disturb or mask detection of early and small inflammation foci in the lungs. However, the relatively fast clearance of radiolabeled autologous leukocytes from the lungs is compatible with PET of infectious foci in such area within a useful time window when using ^{18}F (up to 2 h) (*32*). Finally, the lower uptake of ^{18}F-FDG–WBCs in the brain is most likely a result of reduced diffusion exerted by the BBB. This finding also has strong implications in the clinical setting, as BBB permeability dramatically increases

during inflammatory processes in the brain. In fact, finding high accumulation of labeled WBCs in the brain is a well-known, sensitive indicator of inflammatory disease with local disruption of the BBB (*35*).

CONCLUSION

The data obtained in the present study confirm (a) that accumulation of ^{18}F-FDG–WBCs at the site of inflammation is not simply due to accumulation of free ^{18}F-FDG that might have been released from the radiolabeled WBCs in vivo after their administration and (b) that the enhanced imaging properties of ^{18}F-FDG–WBCs over ^{18}F-FDG might have clinical implications.

REFERENCES

1. Ma LD, Frassica FJ, Bluemke DA, Fishman EK. CT and MRI evaluation of musculoskeletal infection. *Crit Rev Diagn Imaging.* 1997;38:535–568.
2. Roitt IM, Delves PJ. *Essential Immunology.* 10th ed. Oxford, UK: Blackwell Scientific; 2001:164–176.
3. Antony VB, Godbey SW, Kunkel SL, et al. Recruitment of inflammatory cells to the pleural space: chemotactic cytokines, IL-8, and monocyte chemotactic peptide-1 in human pleural fluids. *J Immunol.* 1993;151:7216–7223.
4. Datz FL. In-111-labeled leukocytes for detection of infection: current status. *Semin Nucl Med.* 1994;24:92–109.
5. Palestro CJ, Torres MA. Radionuclide imaging in orthopedic infections. *Semin Nucl Med.* 1997;27:334–345.
6. Thakur ML, Seifert CL, Madsen MT, et al. Neutrophil labeling: problems and pitfalls. *Semin Nucl Med.* 1984;14:107–117.
7. Syrjala MY, Valtonen V, Liewendahl K, Myllyla G. Diagnostic significance of indium-111 granulocyte scintigraphy in febrile patients. *J Nucl Med.* 1987;28:155–160.
8. Ichiya Y, Kuwabara Y, Sasaki M, et al. FDG-PET in infectious lesions: the detection and assessment of lesion activity. *Ann Nucl Med.* 1996;10:185–191.
9. Pio BS, Byrne FR, Aranda R, et al. Noninvasive quantification of bowel inflammation through positron emission tomography imaging of 2-deoxy-2-[18F]-fluoro-D-glucose-labeled white blood cells. *Mol Imaging Biol.* 2003;5:271–277.
10. Cotran RS, Kumar V, Robbins SL. Inflammation and repair. In: Cotran RS, Kumar V, Robbins SL, eds. *Pathologic Basis of Disease.* 5th ed. Philadelphia, PA: Saunders; 1994:51–92.
11. Kurihara T, Warr G, Loy J, Bravo R. Defects in macrophage recruitment and host defense in mice lacking the CCR2 chemokine receptor. *J Exp Med.* 1997;186:1757–1762.
12. National Institutes of Health, Department of Health, Education, and Welfare. *Guide for the Care and Use of Laboratory Animals.* Publication no. 85-23. Revised 1985. Office of Science and Health Reports, Division of Research Resources/NIH: Bethesda, MD; 1985.
13. Hamacher K, Coenen HH, Stocklin G. Efficient stereospecific synthesis of no-carrier-added 2-[18F]-fluoro-2-deoxy-D-glucose using aminopolyether supported nucleophilic substitution. *J Nucl Med.* 1986;27:235–238.
14. Forstrom LA, Dunn WL, Mullan BP, Hung JC, Lowe VJ. Biodistribution and dosimetry of [18F]fluorodeoxyglucose labeled leukocytes in normal human subjects. *Nucl Med Commun.* 2002;23:721–725.
15. Paik JY, Lee KH, Byun SS, Choe YS, Kim BT. Use of insulin to improve [18F]-fluorodeoxyglucose labeling and retention for in vivo positron emission tomography imaging of monocyte trafficking. *Nucl Med Commun.* 2002;23:551–557.
16. Zasadny KR, Recker B, Wahl RL. Untreated primary lung and breast cancers: correlation between F-18 FDG kinetic rate constants and findings of in vitro studies. *Radiology.* 1998;207:767–774.
17. Kaim AH, Weber B, Kurrer MO, et al. Autoradiographic quantification of ^{18}F-FDG uptake in experimental soft-tissue abscesses in rats. *Radiology.* 2002;223:446–451.
18. Kim CK, Gupta NC, Chandramouli B, Alavi A. Standardized uptake values of FDG: body surface area correction is preferable to body weight correction. *J Nucl Med.* 1994;35:164–167.
19. McAfee JC. Inflammatory disorders of soft tissues. In: Harbert JC, Eckelman WC, Neumann RD, eds. *Nuclear Medicine: Diagnosis and Therapy.* New York, NY: Thieme Medical Publishers; 1996:881–908.
20. Weisdorf DJ, Craddock PR, Jacob HS. Glycogenolysis versus glucose transport in human granulocytes: differential activation in phagocytosis and chemotaxis. *Blood.* 1982;60:888–893.
21. Ritchie AC. Inflammation. In: Ritchie AC, ed. *Boyd's Textbook of Pathology.* 9th ed. Vol. 1. Philadelphia, PA: Lea & Febiger; 1990:60–82.
22. Boerman OC, Storm G, Oyen WJ, et al. Sterically stabilized liposomes labeled with indium-111 to image focal infection. *J Nucl Med.* 1995;36:1639–1644.
23. Trop M, Schiffrin EJ, Carter EA. Role of neutrophils in the intestinal alterations associated with thermal injury. *Burns.* 1990;5:343–346.
24. Ismail G, Morganroth ML, Todd RF 3rd, Boxer LA. Prevention of pulmonary injury in isolated perfused rat lungs by activated human neutrophils preincubated with anti-Mo1 monoclonal antibody. *Blood.* 1987;4:1167–1174.
25. Osman S, Danpure HJ. The use of 2-[18F]-fluoro-2-deoxy-D-glucose as a potential in vitro agent for labelling human granulocytes for clinical studies by positron emission tomography. *Int J Rad Appl Instrum B.* 1992;19:183–190.
26. Ward PA, Lentsch AB. The acute inflammatory response and its regulation. *Arch Surg.* 1999;134:666–669.
27. Yamada S, Kubota K, Kubota R, Ido T, Tamahashi N. High accumulation of fluorine-18-fluorodeoxyglucose in turpentine-induced inflammatory tissue. *J Nucl Med.* 1995;36:1301–1306.
28. Sugawara Y, Gutowski TD, Fisher S, Brown RS, Wahl RL. Uptake of positron emission tomography tracers in experimental bacterial infections: a comparative biodistribution study of radiolabeled FDG, thymidine, L-methionine, ^{67}Ga-citrate, and ^{125}I-HSA. *Eur J Nucl Med.* 1999;26:333–341.
29. Tahara T, Ichiya Y, Kuwabara Y, et al. High [^{18}F]-fluorodeoxyglucose uptake in abdominal abscesses: a PET study. *J Comput Assist Tomogr.* 1989;13:829–831.
30. Botti C, Negri DR, Seregni E, et al. Comparison of three different methods for radiolabelling human activated T lymphocytes. *Eur J Nucl Med.* 1997;5:497–504.
31. Pallister I, Topley N. Chemiluminescence: comparison of whole blood with isolated polymorphonuclear leukocytes after major trauma. *J Trauma.* 2004;57:347–351.
32. Love C, Opoku-Agyemang P, Tomas MB, et al. Pulmonary activity on labeled leukocyte images: physiologic, pathologic, and imaging correlation. *Radiographics.* 2002;6:1385–1393.
33. Williams JH Jr, Wilson AF, Moser KM. Is lung sequestration of indium-111-labeled granulocytes organ specific? *J Nucl Med.* 1989;9:1531–1537.
34. Doerschuk CM. Mechanisms of leukocyte sequestration in inflamed lungs. *Microcirculation.* 2001;2:71–88.
35. Hartl R, Medary MB, Ruge M, Arfors KE, Ghajar J. Early white blood cell dynamics after traumatic brain injury: effects on the cerebral microcirculation. *J Cereb Blood Flow Metab.* 1997;11:1210–1220.